Zonal wind velocity profiles in the equatorial electrojet derived from phase velocities of type II radar echoes

E. B. Shume and D. L. Hysell
Department of Earth and Atmospheric Sciences, Cornell University, Ithaca, New York, USA

J. L. Chau
Radio Observatorio de Jicamarca, Instituto Geofísico del Perú, Lima, Perú

Received 25 April 2005; revised 2 September 2005; accepted 8 September 2005; published 16 December 2005.

[1] Zonal wind profiles in the daytime equatorial electrojet are inferred from the Doppler shifts of type II radar echoes observed at the Jicamarca Radio Observatory (JRO) in Perú. The inference is based on a three-dimensional electrostatic potential model. The model includes anomalous effects and is constrained by radar and magnetometer data. The amplitude and phase of the calculated zonal wind profiles are in general agreement with representative wind profiles measured by the WINDII instrument on board the Upper Atmosphere Research Satellite (UARS). The calculated winds also have the same general characteristics as zonal wind profiles measured by rocket-borne chemical release experiments. However, the magnitude of the latter are larger than the former. The temporal behavior of the calculated zonal winds suggests a downward phase progression with a roughly semidiurnal period.

Citation: Shume, E. B., D. L. Hysell, and J. L. Chau (2005), Zonal wind velocity profiles in the equatorial electrojet derived from phase velocities of type II radar echoes, *J. Geophys. Res.*, *110*, A12308, doi:10.1029/2005JA011210.

1. Introduction

[2] Midlatitude and high-latitude *E* region winds can be derived from incoherent scatter radar (ISR) ion drift measurements. Near the magnetic equator, however, the ISR technique generally fails due to clutter from plasma irregularities in the equatorial electrojet. This paper presents a technique which utilizes the electrojet irregularities themselves for inferring zonal winds in the equatorial *E* region.

[3] The equatorial electrojet drives a broadband spectrum of field aligned plasma irregularities. Type I and II spectra are radar signatures of the irregularities that are observed if the Farley-Buneman and gradient-drift instabilities are excited [*Farley*, 1985]. The electrojet current which excites the irregularities is mainly driven by the vertical polarization electric field, an outcome of the complex interaction between the horizontal geomagnetic field geometry, the Cowling conductivity, the background zonal electric field, and the zonal winds. The Doppler shifts of the irregularities are related to the polarization electric field, the winds, and the dynamo fields they induce by a linear dispersion relation [*Fejer et al.*, 1975; *Rogister and D'Angelo*, 1978; *Fejer and Kelley*, 1980]. The winds hence modulate the Doppler shifts [*Sato*, 1975; *Balsley et al.*, 1976; *Broche et al.*, 1978; *Devasia and Reddy*, 1995; *Hysell et al.*, 2002]. Doppler shift profiles from the electrojet measured routinely at Jicamarca are therefore a potential source of information about the lower thermosphere winds.

0148-0227/05/2005JA011210$09.00

[4] Ever since type I and II radar echoes were first observed, attempts have been made to infer winds from them. *Balsley et al.* [1976] noted that since the Doppler shifts are function of the winds, the latter can be indirectly inferred from the radar echoes. By analyzing the linear dispersion relation, *Broche et al.* [1978] indicated that not only the winds but also the dynamo fields they generate must be considered. *Reddy et al.* [1987] inferred zonal electric field in the equatorial *E* region in the Indian sector from Doppler shifts of type II echoes, but their inference ignored the effects of the zonal winds. *Devasia and Reddy* [1995] outlined a method to retrieve zonal winds in the equatorial *E* region from type II echoes, but their method has limited applicability since they neglected the effects of the background zonal electric field.

[5] *Hysell et al.* [2002] presented a comprehensive computational three-dimensional (3-D) electrostatic potential model of the electrojet, driven by the NCAR TIME-GCM model winds. They predicted radar data generally consistent with observations but did not solve the inverse problem of inferring winds from radar data. We take up this problem here.

[6] Central question: Given measured Doppler shifts of type II echoes, how can we infer zonal winds in the equatorial electrojet? We have developed a numerical scheme that combines a 3-D electrostatic potential model (which was described by *Hysell et al.* [2002] in a spherical coordinate system) with coherent and incoherent scatter radar and magnetometer data. The model solves for the potential in the low-latitude ionosphere assuming a homogenous zonal wind profile and by incorporating a

background electric field derived from the ISR. Doppler shift profiles of type II echoes are predicted according to the linear theory of electrojet instabilities. The predicted profiles are compared with Doppler profiles measured at the Jicamarca Radio Observatory (JRO) using a 50 MHz radar with an oblique, narrow antenna beam. The zonal wind profile is then tuned for optimal model-data agreement. Magnetometer data are included to account for anomalous effects and thereby constrain the model.

2. 3-D Low-Latitude Potential Model

[7] In this section a 3-D electrostatic potential model of the low-latitude ionosphere and a method of solving the resulting potential equation in a realistic ionosphere are described.

2.1. Fluid Model Description

[8] The Lorenz force, neutral atmosphere motion, **u**, gravity, **g**, and plasma density gradients, ∇n, present in the *E* and *F* region ionosphere give rise to an anisotropic current [*Richmond*, 1973; *Forbes*, 1981]:

$$\begin{aligned}\mathbf{J} = {} & \sigma_P(\mathbf{E}_\perp + \mathbf{u}\times\mathbf{B}) + \sigma_H\hat{\mathbf{b}}\times(\mathbf{E}+\mathbf{u}\times\mathbf{B}) + \sigma_\circ\mathbf{E}_\parallel \\ & - \left(d_P\boldsymbol{\nabla}_\perp n + d_H\boldsymbol{\nabla}n\times\hat{\mathbf{b}} + d_\circ\boldsymbol{\nabla}_\parallel n\right) \\ & + e_P\mathbf{g}_\perp + e_H\mathbf{g}\times\hat{\mathbf{b}} + e_\circ\mathbf{g}_\parallel, \end{aligned} \tag{1}$$

where **E** is the electric field, $\perp$ and $\parallel$ are perpendicular and parallel components, $\hat{\mathbf{b}} \equiv \dfrac{\mathbf{B}}{|\mathbf{B}|}$, and **B** is the geomagnetic field. The Pedersen, Hall, and direct conductivities are shown below, respectively. The gyrofrequency Ω_α carries the charge (q_α) of plasma species α, and ν_α is the collision frequency for that species.

$$\sigma_P = \sum_\alpha \frac{n_\alpha q_\alpha \nu_\alpha \Omega_\alpha}{B\left(\Omega_\alpha^2+\nu_\alpha^2\right)}, \quad \sigma_H = \sum_\alpha \frac{-n_\alpha q_\alpha \Omega_\alpha^2}{B\left(\Omega_\alpha^2+\nu_\alpha^2\right)}$$
$$\sigma_\circ = \sum_\alpha \frac{n_\alpha q_\alpha \Omega_\alpha}{B\nu_\alpha}. \tag{2}$$

Coefficients of pressure and gravity driven currents in (1) are

$$\begin{aligned} d_P &= \sum_\alpha \frac{\nu_\alpha^2 q_\alpha}{\Omega_\alpha^2+\nu_\alpha^2} d_\alpha, & e_P &= \sum_\alpha \frac{n_\alpha q_\alpha \nu_\alpha}{\Omega_\alpha^2+\nu_\alpha^2} \\ d_H &= \sum_\alpha \frac{\nu_\alpha \Omega_\alpha q_\alpha}{\Omega_\alpha^2+\nu_\alpha^2} d_\alpha, & e_H &= \sum_\alpha \frac{n_\alpha q_\alpha \Omega_\alpha}{\Omega_\alpha^2+\nu_\alpha^2} \\ d_\circ &= \sum_\alpha q_\alpha d_\alpha, & e_\circ &= \sum_\alpha \frac{n_\alpha q_\alpha}{\nu_\alpha}, \end{aligned} \tag{3}$$

where $d_\alpha = \dfrac{k_B T_\alpha}{m_\alpha \nu_\alpha}$, k_B is Boltzmann's constant, and T_α and m_α are temperature and mass of species α.

[9] To maintain solenoidal ionospheric current, $\boldsymbol{\nabla}\cdot\mathbf{J} = 0$, an electric field, $-\boldsymbol{\nabla}\Phi$ is established, which satisfies

$$\begin{aligned}\nabla\cdot\left(\hat{\Sigma}\cdot\nabla\Phi\right) = {} & \nabla\cdot\Big[\hat{\Sigma}\cdot(\mathbf{E}_\circ + \mathbf{u}\times\mathbf{B}) \\ & - \left(d_P\boldsymbol{\nabla}_\perp n + d_H\boldsymbol{\nabla}n\times\hat{\mathbf{b}} + d_\circ\boldsymbol{\nabla}_\parallel n\right) \\ & + e_P\mathbf{g}_\perp + e_H\mathbf{g}\times\hat{\mathbf{b}} + e_\circ\mathbf{g}_\parallel\Big], \end{aligned} \tag{4}$$

where $\mathbf{E}_\circ$ is the background zonal electric field, Φ is an electrostatic potential, and $\hat{\Sigma}$ is the conductivity tensor. The polarization electric field that drives the electrojet is contained within Φ.

2.2. Numerical Procedures

[10] We seek solution of the elliptic partial differential equation (PDE), (4), in the magnetic dipole coordinate system, (p, q, φ), shown in Figure 1. The dipole coordinates and the associated geometric scale factors, h_p, h_q, and h_φ were described by *Hysell et al.* [2004]. We have employed UCAR's MUDPACK package version 4.0 to solve (4). MUDPACK discretizes linear PDE using finite differences on a rectangular grids. It utilizes multigrid iterative technique that combine Gauss-Seidel iteration with subgrid refinement procedures. By iterating and transferring approximations and corrections at subgrid levels, a good initial guess and rapid convergence at the fine grid level can be achieved. Multigrid iteration requires less storage and computation than direct methods for nonseparable elliptic PDEs [*Adams*, 1998].

[11] The simulation space contains 73, 73, and 37 grid points in the (p, q, φ) coordinates, respectively. It is a segment of the equatorial ionosphere in the American sector centered at the geographic latitude, 12°33′S, and longitude, 283°E. It covers altitudes from 85 to 150 km and is ±10° wide both in latitude and longitude. Effects of a titled dipole are neglected since the declination is nearly zero in this sector.

[12] Given appropriate boundary conditions, the PDE solver calculates the potential at each grid point. Neumann boundary conditions are imposed on the q, φ, and lower p boundaries, and on the upper p boundary, the perturbed electric fields are set assuming a perfectly efficient wind driven dynamo there.

[13] We have initially forced the potential model using the NCAR TIME-GCM zonal winds. In subsequent iterations, wind profiles are set by a fitting procedure described below.

2.3. Input Parameters

[14] Neutral densities and temperatures were derived from the MSIS model [*National Space Science Data Center*, 1990], geomagnetic fields from the IGRF model [*National Space Science Data Center*, 2002], and electron densities, compositions, and temperatures from the IRI model [*National Space Science Data Center*, 2001]. We used ion/electron-neutral collision frequency models from *Richmond* [1972], *Gagnepain et al.* [1977], and the electron-ion collision model from *Nicolet* [1953] and reproduced by *Forbes* [1981]. The collision frequency models are functions of neutral densities and temperatures.

2.3.1. *E* Region Electron Densities

[15] The IRI model joins the *E* region peak and the *D* region by an arbitrary function which does not have observational basis. As a result, it overestimates electron densities there. Since electron density profiles derived from the α Chapman function reproduce *E* region densities measured by a bistatic radar at the JRO [*Shume et al.*, 2005], our model represents *E* region electron densities below the *E* region peak by a Chapman function. Figure 2 (dots) shows an example of such a profile for 22 March

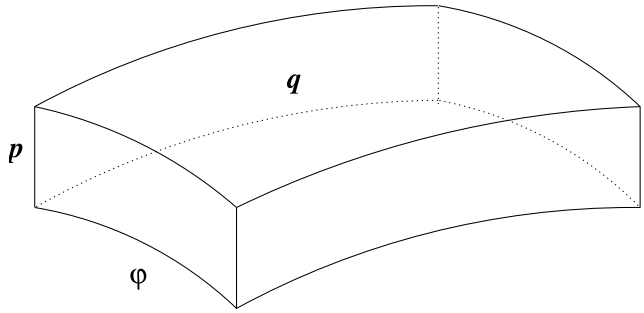

Figure 1. A sketch of the magnetic dipole coordinate system. The three coordinates (p, q, φ) are perpendicular-upward, parallel, and perpendicular-eastward, respectively.

2003, 1100 LT. The profile was derived using *E* region peak density and solar zenith angle data from the IRI model, and the neutral scale height was calculated from MSIS model parameters. The profile also agrees with the FIRI lower ionosphere model [*Friedrich and Torkar*, 2001].

2.3.2. Anomalous Effects

[16] Electric fields due to short wavelength electrojet irregularities can enhance electron transport via anomalous collisions [*St.-Maurice*, 1987; *Ronchi et al.*, 1990]. An effective electron collision frequency will then have classical, ν_e, and an anomalous, ν_e^*, components. *St.-Maurice* [1987] and *Ronchi et al.* [1990] have related ν_e^* to $\left\langle \left| \frac{\delta n}{n} \right|^2 \right\rangle$, the amplitude of the small-scale turbulence strength in the electrojet,

$$\nu_e^* = \frac{\Psi_\circ}{1+\Psi_\circ} \frac{\Omega_e^2}{2\nu_e} \left\langle \left| \frac{\delta n}{n} \right|^2 \right\rangle. \tag{5}$$

[17] Anomalous effects introduce a new $\Psi \equiv \Psi_\circ + \Psi^*$:

$$\Psi = (\nu_e + \nu_e^*) \frac{1}{\Omega_e} \left(\sum_j f_j \frac{\Omega_j}{\nu_j} \right)^{-1}, \tag{6}$$

where f_j is the fractional part of ion species j.

[18] By deriving $\left\langle \left| \frac{\delta n}{n} \right|^2 \right\rangle$ from a rocket experiment [*Pfaff et al.*, 1987], *Ronchi et al.* [1990] reproduced, to a good extent, the shape and magnitude of the equatorial electrojet profile measured in situ. Likewise, the measured electrojet profile was reproduced by *St.-Maurice* [1988]. Our model represents $|\delta n/n|$ by a Gaussian function following *Ronchi et al.* [1990]. The amplitude and width of the Gaussian are tuned in our model until the calculated magnetic field agrees with magnetometer data.

3. Techniques for Inferring Zonal Wind Profiles

[19] Experimentally, type II echo Doppler velocities are measured by an oblique-looking coherent scatter radar at JRO. Theoretically, the Doppler shift of gradient-drift irregularities (shown below), expressed in terms of polarization electric fields, and zonal winds, is predicted by our model. The technique for inferring zonal winds comprises of comparison between the measured and predicted Doppler shifts. The model tunes the winds for best model-data agreement.

3.1. Linear Dispersion Relation

[20] According to the linear theory, the Doppler frequency of electrojet irregularities can be written as [*Fejer et al.*, 1975; *Rogister and D'Angelo*, 1978; *Fejer and Kelley*, 1980],

$$\omega \simeq \frac{\mathbf{k} \cdot (\mathbf{V}_e + \Psi \mathbf{V}_i)}{1+\Psi}, \tag{7}$$

where $\mathbf{k}$ is a wave vector and $\mathbf{V_e}$ and $\mathbf{V_i}$ are electron and ion drifts. Equation (7) describes type II Doppler shift measurements at the JRO but might also describe type I echoes if the ion-acoustic threshold condition holds [*Farley*, 1985].

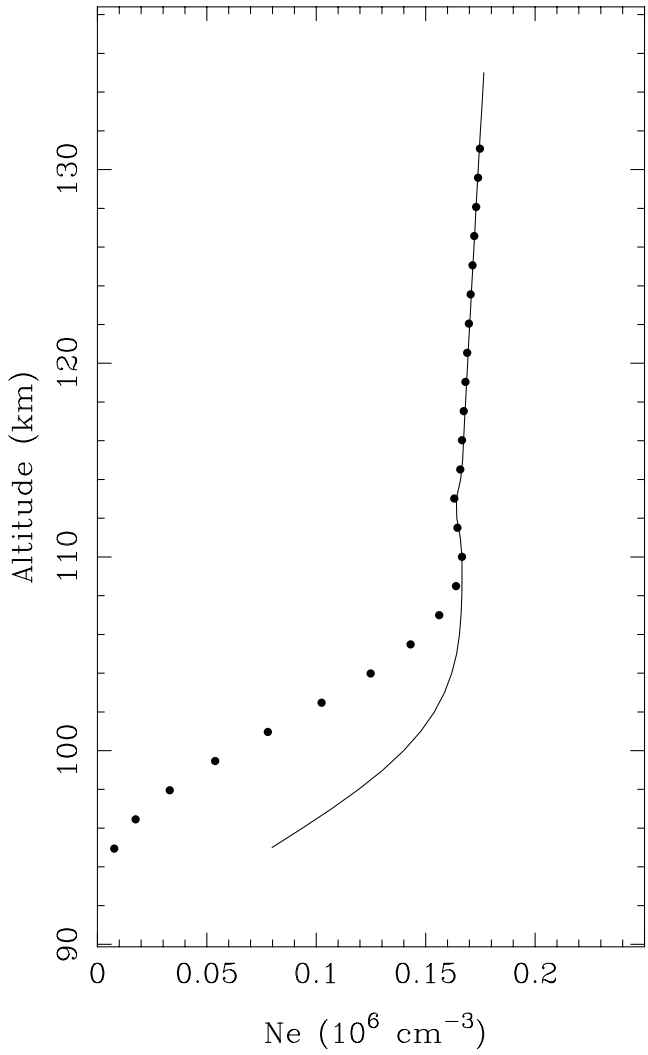

Figure 2. Electron density profiles in the equatorial ionosphere on 22 March 2003, 1100 LT. Dark dots are the electron density profile derived from the α Chapman function, and the solid line represents IRI model densities.

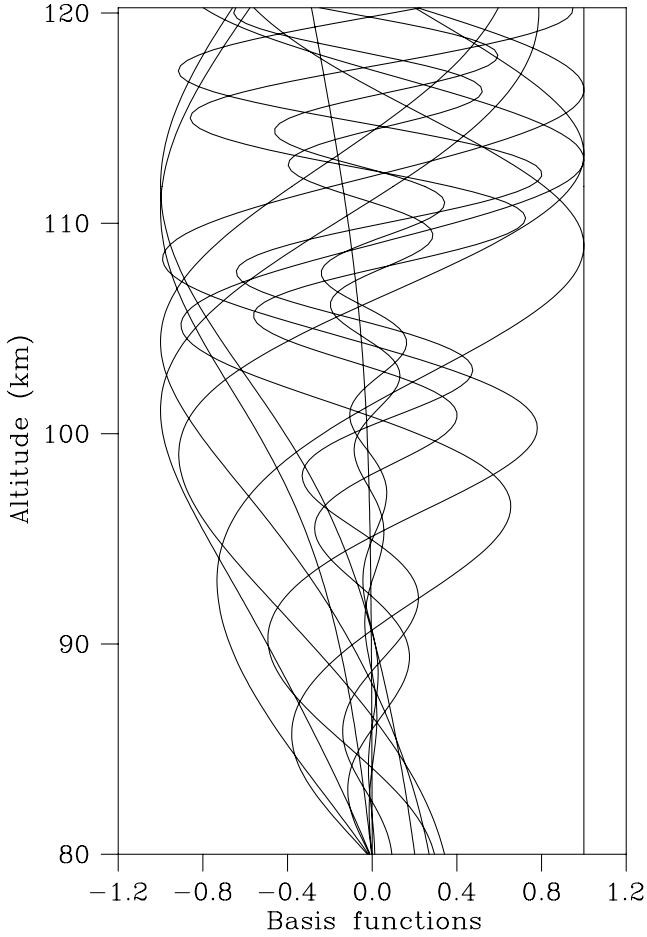

Figure 3. Basis functions used to construct wind profiles. We have used a linear combination of the 14 migrating, nonmigrating, propagating, and nonpropagating tidal modes shown in the figure. They are phases and quadratures of the modes: (1,1), (1,−2), (2,2), (2,4), (2,3), (1,2), and (1,3).

[21] In the electrojet region, since $\nu_e \ll \Omega_e$ and $\nu_i \gg \Omega_i$, $\mathbf{V_e}$ and $\mathbf{V_i}$ can be approximated by the $\mathbf{E} \times \mathbf{B}$ drift and wind velocity, respectively. Consequently, (7) becomes, with β the radar zenith angle,

$$\frac{\omega}{k} \simeq \frac{\sin\beta}{B(1+\Psi)}\left[\cot\beta\left(\frac{1}{h_\varphi}\frac{\partial\Phi}{\partial\varphi} - E_\circ\right) - \frac{1}{h_p}\frac{\partial\Phi}{\partial p} - \Psi u B\right]. \quad (8)$$

[22] Owing to lack of reliable vertical wind data, the influence of vertical winds on the electrojet is ignored in our wind estimation. Meanwhile, we know from theoretical analysis of momentum and mass continuity equations that vertical air motion is much smaller than horizontal air motion. The influence of meridional winds is ignored as well, since they cause negligible dynamo effects near the magnetic equator.

3.2. Inferring Zonal Wind Profiles

[23] The model estimates zonal winds iteratively. Winds are expressed in terms of linearly independent basis functions, shown in Figure 3, which are related to the vertical extensions of the Hough functions described by *Chapman and Lindzen* [1970]. The initial wind profile is based on NCAR TIME-GCM model predictions. Doppler shift profiles are then predicted using (8) and compared with measurements. Iteration continues by updating the winds, adding a function of the difference between the measured and predicted Doppler profiles each time. Model-data agreement is seen to improve rapidly, first at low altitudes and later higher up. Iteration ceases when the χ^2 difference between modeled and measured Doppler shifts falls below a threshold, at which point the zonal wind profile has been estimated.

4. Results and Discussion

4.1. Constraints

[24] We have run the model for 22 March 2003, 1100 LT condition. For this run, the background electric field ($E_\circ$) was set to 0.4 mV/m. This electric field value is extracted from ISR average vertical plasma drift data. Average vertical drifts derived from ISR agree with vertical drifts from the so called 150 km echoes at JRO [*Chau and Woodman*, 2004]. Below 150 km, however, we expect the zonal electric field to vary with altitude. The strategy we have adopted to get the proper $E_\circ$ is to make an initial guess and modify the guess such that the total calculated electric field at the top of the simulation space, $E_\circ - \frac{1}{h_\varphi}\frac{\partial\Phi}{\partial\varphi}$, matches the electric field data derived from ISR, which was 0.4 mV/m for 22 March 2003, 1100 LT.

[25] Our wind estimation was also constrained by magnetometer data from 22 March 2003, 1100 LT. The net measured horizontal (H) and vertical (Z) components from magnetograms were obtained by subtracting the H and Z components measured at Jicamarca (2° magnetic north) from those measured at Piura (6°8′ magnetic north). The resulting H and Z components were again subtracted from the nighttime baseline magnetometer records at Jicamarca. This was done to remove current sources save the electrojet, which might cause magnetometer deflections. The calculated H and Z components were compared with their measured counterparts. The magnetic field calculations, along with the wind estimations, are repeated by tuning the turbulence strength until the agreement between the calculated and measured magnetic fields is close. Setting $|\delta n/n|$ to 2%, a value in the range of rocket measurement [*Pfaff et al.*, 1987], the calculated and measured magnetic fields agree well. The calculated (H, Z) = (38,17) nT, and the measured (H, Z) = (40, 21) nT for 22 March 2003, 1100 LT.

[26] We have run the potential model on quarter of an hour intervals from 930 to 1400 LT for the same day. The background electric field is time varying and is updated at each time step according to the Jicamarca drifts database. The wind profiles and magnetic field components were calculated using the procedures described above. We have varied $|\delta n/n|$ from 2 to 5% to force agreement between the calculated and measured H and Z components. Figure 4 shows the results of the magnetic field comparison. Circles and stars are measured and calculated H components, respectively. Crosses and dots are measured and calculated Z components, respectively. As shown by Figure 4, we have to a good extent recovered magnetometer observations using measured electric fields, type II Doppler shifts,

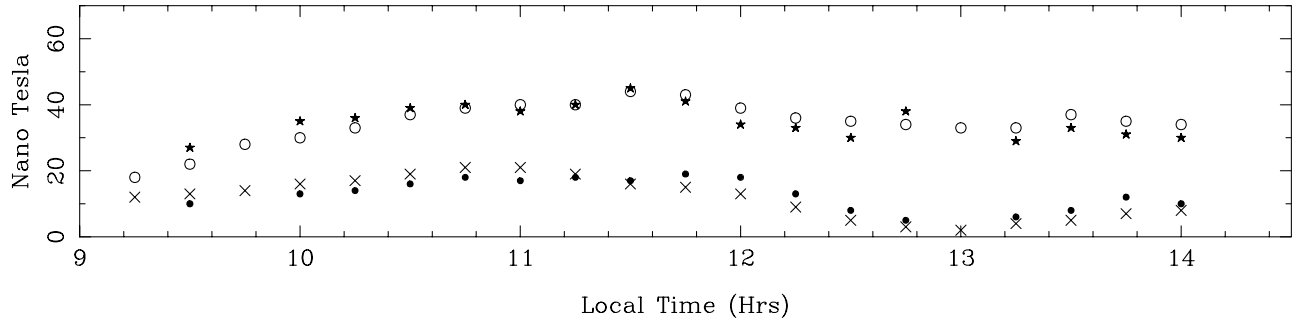

Figure 4. Comparison between the horizontal and vertical components of the measured and calculated magnetic field (nT) on 22 March 2003. Circles are measured horizontal components, stars are calculated horizontal components, the crosses are measured vertical components, and dots are calculated vertical components.

incorporating reasonable turbulence strength parameters, and assuming plausible winds.

4.2. Calculated Zonal Wind Profiles

[27] The calculated zonal wind profile (broken line) for 22 March 2003, 1100 LT is plotted in Figure 5. The coordinate convention used here is that positive values imply eastward winds but westward propagating electrojet waves. Also shown are measured (circles with error bars) and calculated (solid line) type II echo Doppler shifts. The calculated phase velocities have clearly reproduced the measured profile. This agreement and the magnetic field

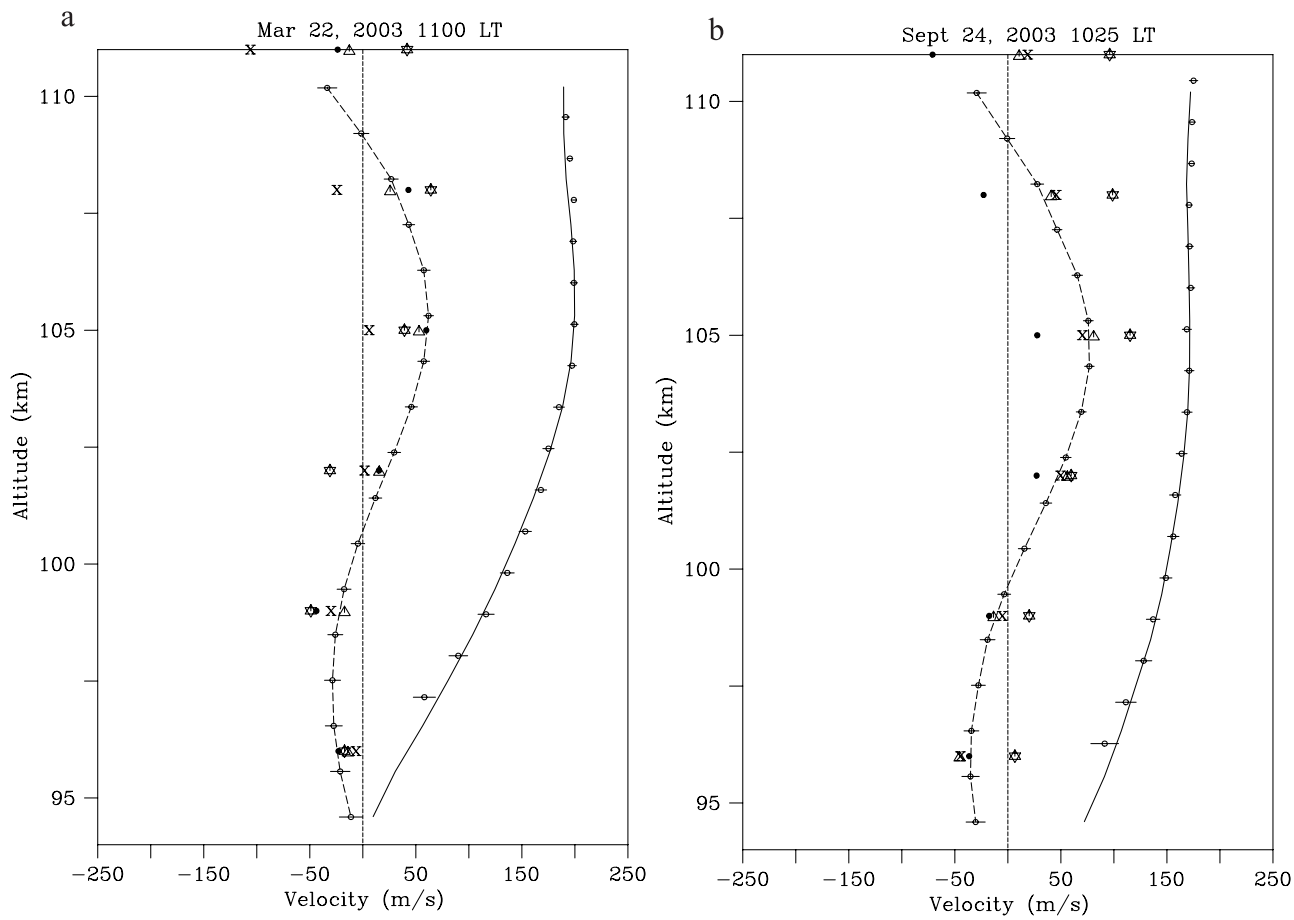

Figure 5. Calculated zonal wind profile (broken line with error bars) in the equatorial *E* region. A comparison of the calculated winds with winds measured by WINDII instrument on board the UARS satellite (crosses, stars, dots, and triangles) are also shown. The solid line and error bars with circles show the predicted and measured Doppler velocity of type II echoes, respectively.

comparison mentioned above suggest that the calculated winds are representative of zonal wind profiles in the equatorial electrojet region.

[28] The calculated wind profile shown in Figure 5 (22 March 2003, 1100 LT) has a magnitude of about 60 m/s directed eastward at the center of the electrojet. It is directed westward with a relatively smaller magnitude at the lower edge of the electrojet. Eastward winds slow down gradient drift waves during the day by opposing the driving vertical polarization electric fields, whereas westward winds speed up the waves, as shown by (8). The calculated wave phase speed around 106 km would have been faster had the magnitude of the eastward wind been smaller. Westward winds were needed in the bottomside to drive the waves in the collisional lower electrojet region. In the figure, we have also shown a comparison of the calculated winds with a wind data set measured by the WINDII instrument on board the Upper Atmosphere Research Satellite (UARS). UARS had a nearly circular orbit at 585 km inclined at 57° to the equator. The instruments on board were mounted at 90° to the spacecraft velocity vector and could see to 80° latitude in one hemisphere and to 34° to the other [*Reber et al.*, 1993]. The WINDII instrument recorded zonal and meridional wind components over a large span of latitudes, longitudes, and altitudes. The data used in our study were recorded by the WINDII instrument when it looked within ±5° of the latitude and longitude of the Jicamarca radar site. The data correspond to 19 September 1992 early afternoon (crosses), 31 October 1992 late morning (stars), and 26 November 1992 early afternoon (dots and triangles). The local time and solar flux level of the data are comparable with our model run conditions. The calculated wind profile has the same envelope and phasing as the WINDII wind profiles as shown in Figure 5. The amplitude of the calculated zonal wind is also consistent with the 26 November 1992 WINDII data.

[29] The model was also run for a 24 September 2003, 1025 LT condition. For this run, a background electric field was set to 0.475 mV/m. The resulting wind profile is shown in Figure 5. It has amplitude and phase comparable to the 22 March 2003 calculated wind profile. The phase and amplitude agreement with WINDII data is again good. The WINDII data here were from 4 September 1995 early afternoon (dots), 13 November 1996 late morning (stars), 14 November 1995 late morning (crosses and triangles). The two instances (22 March and 24 September 2003) argue that the wind profiles produced by our procedure reveal the attributes of local wind profiles in the electrojet.

4.3. Uniqueness and Sensitivity

[30] The calculated potential at a given altitude is a function of the winds not only at that altitude but also all altitudes below. Winds do not generate dynamo fields in the lower edge of the electrojet (below about 93 km), however, since conductivities drop significantly there. Zonal winds could be uniquely inverted from Doppler velocity data since winds have negligible dynamo effect below altitudes for which we have Doppler shift data. This same argument was also used by *Devasia and Reddy* [1995].

[31] We have conducted an ensemble analysis of the wind calculation to examine the sensitivity of the employed numerical procedures. We have examined the responses of the calculated wind profiles to variations of the Doppler and electric field data within the uncertainties of their respective measurements. The results of the analysis are displayed by the error bars on the calculated wind profiles (broken lines) in Figure 5, the rms spread is about 8 m/s on average.

4.4. Temporal Behavior

[32] The temporal characteristics of the calculated zonal wind profiles for 22 March and 24 September 2003 are displayed in Figure 6. Each curve represents the specific local time shown by the legend on the top corners of the figures. The wind oscillations in both days have an average vertical wavelength of about 15 km, and the phases show a slow descent. The 22 March and 24 September 2003 wind profiles propagate downward 4.5 km in about 5 hours, and 3 km in about $2\frac{3}{4}$ hours, respectively. The phase of the 22 March 2003 wind makes approximately one full oscillation in about 13 hours or about two oscillations in a day, and that of the 24 September 2003 phase makes one complete oscillation in about $13\frac{1}{2}$ hours. The downward phase progression is therefore nearly semidiurnal. Using ISR ion line drift measurements at Arecibo, *Harper et al.* [1976] have shown eastward and southward winds to have a downward propagation pattern with approximate periods within the range of 10–13 hours. *Bernard and Spizzichino* [1971] have shown wind and temperature data between 95 and 140 km derived from ISR experiment at Nancay (France) to have a dominant semidiurnal periodicity with downward phase propagation. *Bernard* [1974] has also found semidiurnal propagating *E* region tidal modes using ISR measurements in Saint Santin (France). The phase oscillations of the calculated as well as the radar measured wind profiles have therefore semidiurnal period with the phase progressing downward. However, the vertical wavelength of the winds measured by *Bernard and Spizzichino* [1971] and *Bernard* [1974] are about three times larger than the wavelength calculated by our procedure. On the other hand, the model wind results have the same phasing and comparable wavelength as the *E* region zonal wind profiles measured by rocket chemical release experiments conducted in the equatorial ionosphere [*Larsen*, 2002; *Larsen and Odom*, 1997], although the rocket wind data have larger amplitude. The discrepancy in amplitude of the two wind estimates may lie in the inherent differences between the radar and rocket experiments. The calculated wind profiles were extracted from spatially and temporally averaged Doppler velocities of type II radar echoes, whereas each point of the wind profiles measured by the rocket chemical release experiment was sampled from single spatial location instantly.

5. Conclusion

[33] We have reported on zonal wind profiles in the equatorial electrojet region in the South American sector extracted from Doppler shifts of type II radar echoes measured at JRO. Zonal wind profiles are retrieved by combining a 3-D electrostatic potential model with predictions and measurements of type II echoes in the equatorial electrojet. Our model calculations are consistent with mag-

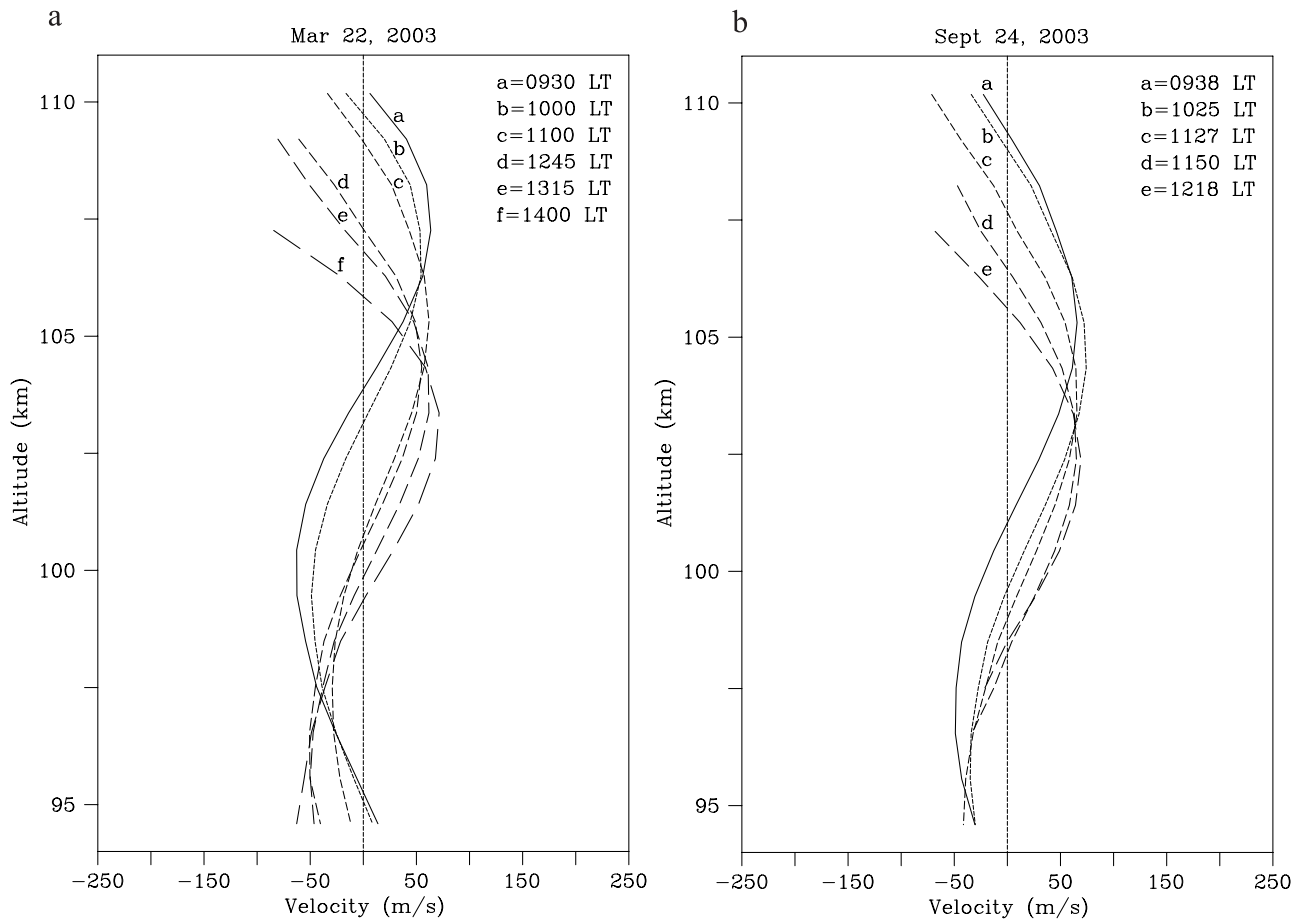

Figure 6. Temporal characteristics of the calculated zonal wind profiles on 22 March and 24 September 2003.

netometer and vertical plasma drift data measured by ISR at JRO and incorporate anomalous effects. The magnitude and phasing of the calculated zonal wind profiles agree well with winds measured by the WINDII instrument on board UARS. It is evident from the temporal properties of the calculated winds that the phase progresses downward with a period of about half a day which might be a signature of the semidiurnal tide. The downward phase progression of the zonal winds appear to influence the electrodynamics of the local plasma by modulating the magnitude and direction of the polarization electric fields through a dynamo mechanism. Concurrent bistatic and oblique coherent scatter radar experiments would be conducted at Jicamarca to investigate the influences of the downward phase progression of the winds might have on the *E* region plasma density profiles and plasma instabilities.

[34] **Acknowledgments.** The authors would like to thank John Emmert of NRL/George Mason University for providing us with the WINDII data. This work was supported by the National Science Foundation through cooperative agreement ATM-0432565 to Cornell University and by NSF grant ATM-0226235 to Cornell University. The Jicamarca Radio Observatory is operated by the Instituto Geofísico del Perú, Ministry of Education, with support from the NSF cooperative agreements just mentioned. The help of the staff is much appreciated. MUDPACK (Multigrid Software for Elliptic PDEs) version 4 (1998) used for this research (copyright John C. Adams) was obtained from UCAR which is sponsored by NSF.

[35] Arthur Richmond thanks Meers Oppenheim and Jean-Pierre St-Maurice for their assistance in evaluating this paper.

References

Adams, J. C. (1998), MUDPACK: Multigrid software for elliptic partial differential equations, Univ. Corp. for Atmos. Res., Boulder, Colo. (Available at http://www.scd.ucar.edu/css/software/mudpack)

Balsley, B. B., B. G. Fejer, and D. T. Farley (1976), Radar measurements of neutral winds and temperatures in the equatorial *E* region, *J. Geophys. Res.*, *81*, 1457.

Bernard, R. (1974), Tides in the *E* region observed by incoherent scatter over Saint Santin, *J. Atmos. Terr. Phys.*, *36*, 1105.

Bernard, R., and A. Spizzichino (1971), Semi-diurnal wind and temperature oscillations in the *E* region observed by the Nancay incoherent scatter experiment, *J. Atmos. Terr. Phys.*, *33*, 1345.

Broche, P., M. Crochet, and J. Gagnepain (1978), Neutral winds and phase velocity of the instabilities in the equatorial electrojet, *J. Geophy. Res.*, *83*, 1145.

Chapman, S., and R. S. Lindzen (1970), *Atmospheric Tides: Thermal and Gravitational*, Gordon and Breach, New York.

Chau, J. L., and R. F. Woodman (2004), Daytime vertical and zonal velocities from 150-km echoes: Their relevance to *F* region dynamics, *Geophys. Res. Lett.*, *31*, L17801, doi:10.1029/2004GL020800.

Devasia, C. V., and C. A. Reddy (1995), Retrieval of east-west wind in the equatorial electrojet from local wind-generated electric field, *J. Atmos. Terr. Phys.*, *57*, 1233.

Farley, D. T. (1985), Theory of equatorial electrojet plasma waves: New developments and current status, *J. Atmos. Terr. Phys.*, *42*, 729.

Fejer, B. G., and M. C. Kelley (1980), Ionospheric Irregularities, *Rev. Geophys.*, *18*, 401.

Fejer, B. G., D. T. Farley, B. B. Balsley, and R. F. Woodman (1975), Vertical structure of the VHF backscattering region in the

equatorial electrojet and the gradient drift instability, *J. Geophys. Res.*, *80*, 10.
Forbes, J. M. (1981), The equatorial electrojet, *Rev. Geophys.*, *19*, 469.
Friedrich, M., and K. M. Torkar (2001), FIRI: A semiempirical model of the lower ionosphere, *J. Geophys. Res.*, *106*, 21,409.
Gagnepain, J., M. Crochet, and A. D. Richmond (1977), Comparion of equatorial electrojet models, *J. Atmos. Terr. Phys.*, *39*, 1119.
Harper, R. M., R. H. Wand, C. J. Zamlutti, and D. T. Farley (1976), E region ion drifts and winds from incoherent scatter measurements at Arecibo, *J. Geophys. Res.*, *105*, 25.
Hysell, D. L., J. L. Chau, and C. G. Fesen (2002), Effect of large scale horizontal winds on the equatorial electrojet, *J. Geophys. Res.*, *107*(A8), 1214, doi:10.1029/2001JA000217.
Hysell, D. L., J. Chun, and J. L. Chau (2004), Bottom-type scattering layers and equatorial spread *F*, *Ann. Geophys.*, *22*, 4061.
Larsen, M. F. (2002), Winds and shears in the mesosphere and lower thermosphere: Results from four decades of chemical release wind measurements, *J. Geophys. Res.*, *107*(A8), 1215, doi:10.1029/2001JA000218.
Larsen, M. F., and C. D. Odom (1997), Observation of altitudinal and latitudinal E-region neutral wind gradients near sunset at the magnetic equator, *Geophys. Res. Lett.*, *24*, 1711.
Nicolet, M. (1953), The collision frequency of electrons in the ionosphere, *J. Atmos. Terr. Phys.*, *3*, 200.
National Space Science Data Center (1990), *MSIS-E-90 Atmosphere Model*, Greenbelt, Md. (Available at http://nssdc.gsfc.nasa.gov/space/model/models/msis.html)
National Space Science Data Center (2001), *International Reference Ionosphere: IRI-2001*, Greenbelt, Md. (Available at http://nssdc.gsfc.nasa.gov/space/model/models/iri.html)
National Space Science Data Center (2002), *IGRF Geomagnetic Field Model*, Greenbelt, Md. (Available at http://nssdc.gsfc.nasa.gov/space/model/models/igrf.html)
Pfaff, R. F., M. C. Kelley, E. Kudeki, B. G. Fejer, and K. D. Baker (1987), Electric field and plasma density measurements in the strongly driven daytime equatorial electrojet: 2. The unstable layer and gradient drift waves, *J. Geophys. Res.*, *92*, 13,578.
Reber, C. A., C. E. Trevathan, R. J. McNeal, and M. R. Luther (1993), The Upper Atmosphere Research Satellite (UARS) mission, *J. Geophys. Res.*, *98*, 10,643.
Reddy, C. A., B. T. Vikramkumar, and K. S. Viswanathan (1987), Electric fields and currents in the equatorial electrojet deduced from VHF radar observations, I, A method of estimating electric fields, *J. Atmos. Terr. Phys.*, *49*, 183.
Richmond, A. D. (1972), Numerical model of the equatorial electrojet, *Tech. Rep. AFCRL-72-0668, ERP 421*, Air Force Cambridge Res. Lab., Hanscom AFB, Bedford, Mass.
Richmond, A. D. (1973), Equatorial electrojet-I. Development of a model including winds and instabilities, *J. Atmos. Terr. Phys.*, *35*, 1083.
Rogister, A., and N. D'Angelo (1978), Type II irregularities in the electrojet, *J. Geophys. Res.*, *75*, 3879.
Ronchi, C., R. N. Sudan, and P. L. Similon (1990), Effect of short-scale turbulence on kilometer wavelength irregularities in the equatorial electrojet, *J. Geophys. Res.*, *95*, 189.
Sato, T. (1975), Neutral winds and electrojet irregularities, *J. Geophys. Res.*, *80*, 2835.
Shume, E. B., D. L. Hysell, and J. L. Chau (2005), Electron density profiles in the equatorial E region ionosphere derived from bistatic radar experiment at Jicamarca, *Geophys. Res. Lett.*, *32*, L01107, doi:10.1029/2004GL021715.
St.-Maurice, J. P. (1987), A unified theory of anomalous resistivity and Jould heating effects in the presence of ionospheric *E* region irregularities, *J. Geophys. Res.*, *92*, 4533.
St.-Maurice, J. P. (1988), Wave-induced diffusion in the turbulent *E* region, in *Polar Cap Dynamics and High Latitude Turbulence*, *SPI Conf. Proc. and Reprint Ser.*, vol. 8, edited by T. Chang, G. B. Crew, and J. R. Jasperse, pp. 323–338, Scientific, Gainesville, Fla.

J. L. Chau, Radio Observatorio de Jicamarca, Instituto Geofisico del Peru, Apartado 13-0207, Lima 13, Perú. (jchau@jro.igp.gob.pe)
D. L. Hysell and E. B. Shume, Department of Earth and Atmospheric Sciences, Cornell University, 2108 Snee Hall, Ithaca, NY 14853, USA. (dlh37@cornell.edu; ebs27@cornell.edu)